

2 **Energy reconstruction of hadronic showers**
3 **at the CERN PS and SPS using the**
4 **Semi-Digital Hadronic Calorimeter**

The CALICE Collaboration

D. Boumediene

Université Clermont Auvergne, Université Blaise Pascal, CNRS/IN2P3, LPC, 4 Av. Blaise Pascal, TSA/CS 60026, F-63178 Aubière, France

A. Pingault, M. Tytgat

Ghent University, Department of Physics and Astronomy, Proeftuinstraat 86, B-9000 Gent, Belgium

Y. W. Baek, D-W. Kim,* S. C. Lee, B. G. Min, S. W. Park

Gangneung-Wonju National University Gangneung 25457, South Korea

Y. Deguchi, K. Kawagoe, Y. Miura, R. Mori, I. Sekiya, T. Suehara, T. Yoshioka

Department of Physics and Research Center for Advanced Particle Physics, Kyushu University, 744 Motoooka, Nishi-ku, Fukuoka 819-0395, Japan

L. Caponetto, C. Combaret, G. Garillot, G. Grenier, J-C. Ianigro, T. Kurca, I. Laktineh^a, B. Liu^a, B. Li, N. Lumb, H. Mathez, L. Mirabito, A. Steen[†]

Univ Lyon, Univ CLaude Bernard Lyon 1, CNRS/IN2P3, IP2I Lyon, F-69622 Villeurbanne, France

E. Calvo Alamillo, C. Carrillo, M.C. Fouz, H. Garcia Cabrera, J. Marin, J. Navarrete, J. Puerta Pelayo, A. Verdugo

CIEMAT, Centro de Investigaciones Energeticas, Medioambientales y Tecnologicas, Madrid, Spain

F. Corriveau

Department of Physics, McGill University, Ernest Rutherford Physics Bldg., 3600 University Ave., Montréal, Québec Canada H3A 2T8

L. Emberger, C. Graf, L.M.S de Silva, F. Simon, C. Winter

Max-Planck-Institut für Physik, Föhringer Ring 6, D-80805 Munich, Germany

J. Bonis, D. Breton, P. Cornebise, A. Gallas, J. Jeglot, A. Irlès, J. Maalmi, R. Pöschl, A. Thiebault, F. Richard, D. Zerwas

Universit Paris-Saclay, CNRS/IN2P3, IJCLab, 91405 Orsay, France

**J. Cvach, M. Janata, M. Kovalcuk, J. Kvasnicka, I. Polak, J. Smolik, V. Vrba,
J. Zalesak, J. Zuklin**

*Institute of Physics, The Czech Academy of Sciences, Na Slovance 2, CZ-18221 Prague 8,
Czech Republic*

**Y.Y. Duan, S. Li, J. Guo, J.F. Hu, F. Lagarde, B. Liu, Q.P. Shen, X. Wang,
W.H. Wu, H.J. Yang, Y.F. Zhu**

*Tsung-Dao Lee Institute, Institute of Nuclear and Particle Physics, School of Physics and
Astronomy, Shanghai Jiao Tong University, Key Laboratory for Particle Physics,
Astrophysics and Cosmology (Ministry of Education), Shanghai Key Laboratory for
Particle Physics and Cosmology, 800 Dongchuan Road, Shanghai, 200240, P. R. China*

L. Emberger, C. Graf, L.M.S de Silva, F. Simon, C. Winter

Max-Planck-Institut für Physik, Föhringer Ring 6, D-80805 Munich, Germany

^a *Corresponding authors*

E-mail: laktineh@in2p3.fr, liubinglove7@gmail.com

Calice Collaboration

ABSTRACT: The CALICE Semi-Digital Hadronic CALorimeter (SDHCAL) is the first technological prototype in a family of high-granularity calorimeters developed by the CALICE Collaboration to equip the experiments of future lepton colliders. The SDHCAL is a sampling calorimeter using stainless steel for absorber and Glass Resistive Plate Chambers (GRPC) as a sensitive medium. The GRPC are read out by $1\text{ cm} \times 1\text{ cm}$ pickup pads combined to a multi-threshold electronics. The prototype was exposed to hadron beams in both the CERN PS and the SPS beamlines in 2015 allowing the test of the SDHCAL in a large energy range from 3 GeV to 80 GeV. After introducing the method used to select the hadrons of our data and reject the muon and electron contamination, we present the energy reconstruction approach that we apply to the data collected from both beamlines and we discuss the response linearity and the energy resolution of the SDHCAL. The results obtained in the two beamlines confirm the excellent SDHCAL performance observed with the data collected with the same prototype in the SPS beamline in 2012. They also show the stability of the SDHCAL in different beam conditions and different time periods.

*Now at Seoul National University Hospital

†Now at NTU

7 Contents

8	1. Introduction	1
9	2. Simulation	2
10	3. Pion events selection	3
11	3.1 Electron contamination rejection using Boosted Decision Tree (BDT)	4
12	3.1.1 BDT input variables	4
13	3.1.2 Training and testing details of the BDT	8
14	3.2 Muon contamination rejection	9
15	4. Energy reconstruction	11
16	4.1 Energy resolution and linearity	13
17	5. Uncertainties estimation	15
18	6. Conclusion	17
19	7. Acknowledgements	18

21 1. Introduction

22 The Semi-Digital Hadronic CALorimeter (SDHCAL) [1] is the first of a series of tech-
 23 nological high-granularity prototypes developed by the CALICE collaboration. The SD-
 24 HCAL is a sampling calorimeter using stainless steel for absorber and Glass Resistive
 25 Plate Chambers (GRPC) for its sensitive medium. The SDHCAL is designed to be as
 26 compact as possible with its mechanical structure being part of the absorber. The GRPC
 27 and the readout electronics are conceived to achieve minimal dead zones in the SDHCAL.
 28 This design renders the SDHCAL optimal for the application of the Particle Flow Algo-
 29 rithm (PFA) techniques [2, 3, 4].

30 The SDHCAL (1) comprises 48 active layers, each of them equipped with a $1\text{ m} \times 1\text{ m}$
 31 GRPC and an Active Sensor Unit (ASU) of the same size hosting on one side (the one in
 32 contact with the GRPC) pickup pads of $1\text{ cm} \times 1\text{ cm}$ size each and 144 HARDROC2
 33 ASICs [5] on the other side (Fig. 2). The GRPC and the ASU are assembled within
 34 a cassette made of two stainless steel plates, 2.5 mm thick each. The 48 cassettes are

35 inserted in a self-supporting mechanical structure made of 49 plates, 15 mm thick each,
36 of the same material as the cassettes, bringing the total absorber thickness to 20 mm per
37 layer. The empty space between two consecutive plates is 13 mm to allow the insertion
38 of one cassette of 11 mm thickness. In total, the SDHCAL represents about 6 interaction
39 lengths λ_I . The HARDROC2 ASIC has 64 channels to read out 64 pickup pads. Each
40 channel has three parallel digital circuits whose parameters can be configured to provide
41 2-bit encoded information per channel indicating if the charge seen by each pad has passed
42 any of the three different thresholds associated to each digital circuit. This multi-threshold
43 readout is used to improve on the energy reconstruction of hadronic showers at high energy
44 (> 30 GeV) with respect to the simple binary readout mode as explained in Ref. [6].

45 The SDHCAL was exposed to different kinds of particles at the CERN SPS beamline
46 in 2012 and its performance was studied in the the energy range above 10 GeV [6] since
47 lower particle energy values are difficult to obtain in the SPS beamline standard configu-
48 rations. To study its performance in different beam conditions and at lower energies, the
49 SDHCAL was exposed to hadrons both in the SPS and PS beamlines in 2015. It was first
50 exposed to negatively charged pion beams of 3, 4, 5, 6, 7, 8, 9, 10 and 11 GeV at the PS
51 beamline and then to positively charged hadrons of 10, 20, 30, 40, 50, 60, 70 and 80 GeV
52 at the SPS beamline. In both cases, about 10000 events were collected for each energy
53 point.

54 In this paper, section 2 gives the details of the collected beam data as well as the
55 samples of simulated events used for comparison. The pion selection and the muon and
56 electron contamination rejection using the MultiVariate Analysis (MVA) technique known
57 as Boosted Decision Trees (BDT) to separate pion and electron showers is given in sec-
58 tion 3. Energy reconstruction of the selected pion events is discussed in section 4. Finally,
59 in section 5 we present the uncertainties related to the energy reconstruction of the col-
60 lected data.

61 2. Simulation

62 The simulation model of SDHCAL, based on Geant4.9.6 toolkit package [7], was devel-
63 oped including the interactions of different kinds of particles such as muons, electrons and
64 pions in the SDHCAL prototype. The simulation takes into account the operation condi-
65 tions of the GRPC to which an effective high voltage of 7.2 kV was applied. It uses the
66 same values of 0.114, 5 and 15 pC that are used by the SDHCAL readout system for the
67 first, the second and the third threshold respectively.

68 Among the different Geant4 physics lists that were used to compare the simulation
69 with the beam data collected in 2012, FTF_BIC was found to provide the best agree-
70 ment [8]. Therefore, we use this physics list in this work to simulate events with different
71 kinds of particles having the same energies and impinging on the prototype in the same
72 area as those to which the SDHCAL was exposed during the beam test campaigns at the
73 SPS and PS beamlines. The simulated events are then used to optimize the selection of

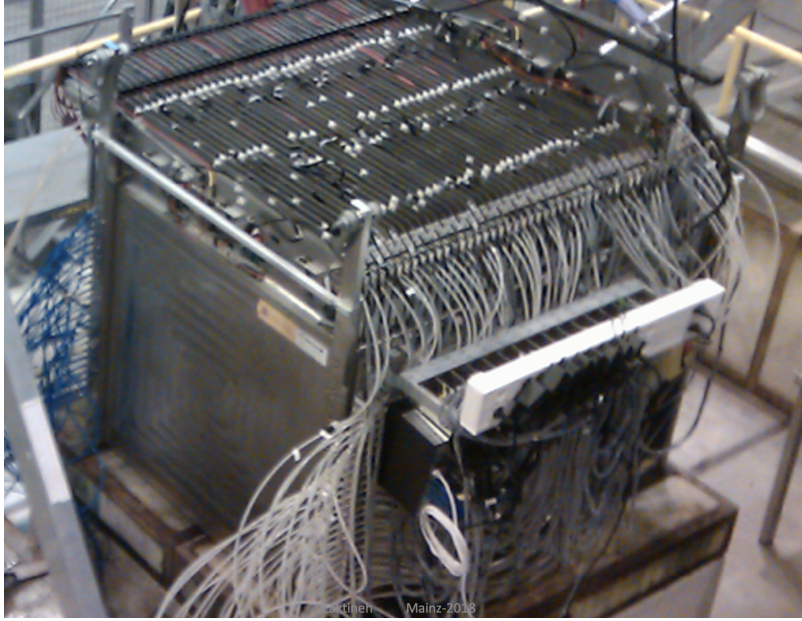


Figure 1. A picture of the SDHCAL prototype in beam test.

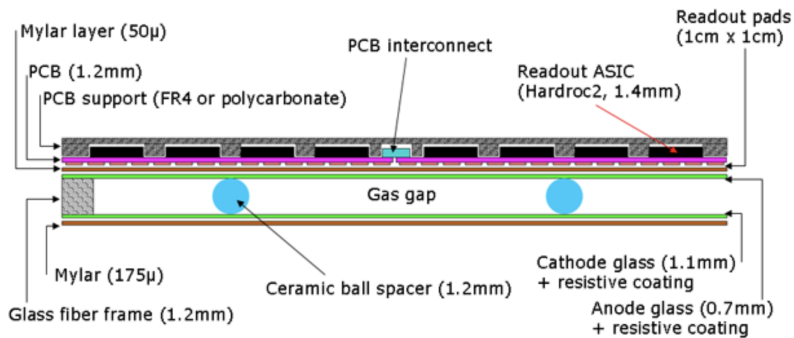


Figure 2. Cross-section of one of the prototype's 48 active layers.

74 pions in data by rejecting muon and electron beam contamination. They are also used
 75 to estimate possible biases that may influence the data energy reconstruction of hadronic
 76 showers in terms of linearity and resolution.

77 **3. Pion events selection**

78 The pion samples of both SPS and PS beams are contaminated by two kinds of particles:
 79 electrons and muons. The muon contamination exists in all samples from 3 to 80 GeV.
 80 This includes two different types of muons: cosmic muons and beam muons. The latter
 81 are generated by pions decaying before arriving at the prototype. Concerning the electron
 82 contamination, it is negligible in pion samples from 6 to 11 GeV in the PS pion beam but
 83 still present in the energy range below 6 GeV at the level of a few percent of the beam

84 content. The electron contamination is also present in the SPS pion beam, especially in
 85 the energy range between 10 and 50 GeV [6]. The muon rejection is rather easy due to
 86 their track-like shape that distinguishes them clearly from the hadronic showers in the
 87 SDHCAL. The electron rejection is harder. Electron showers, in particular at low energy,
 88 are similar to the pion ones. Although in both PS and SPS, an electron stopper made of a
 89 few millimeters thick lead plate was used, this does not allow to completely eliminate the
 90 electron contamination. Inspired by Refs. [9, 10], we propose to use the BDT technique to
 91 reject the electron background of our pion samples in an improved way with respect to the
 92 one used in a previous analysis applied to data collected by SDHCAL in 2015 at the SPS
 93 beamline [11] in the energy range between 10 and 80 GeV.

94 **3.1 Electron contamination rejection using Boosted Decision Tree (BDT)**

95 As mentioned in the previous section, for the 6 to 11 GeV pion runs, the electron con-
 96 tamination is negligible in the PS pion beam. However for the 3 to 5 GeV pion runs, the
 97 electron contamination is expected to be present due to the PS beamline structure. There-
 98 fore, it is necessary to check the electron contamination and to eliminate it. Thanks to the
 99 high granularity of the SDHCAL prototype, we can use the BDT method to exploit the
 100 three dimensional shape of both the electromagnetic and the hadronic showers to classify
 101 the electron and pion events in our prototype. The BDT method is one of the most powerful
 102 and widely used in high energy physics for classification tasks. The TMVA package [12]
 103 contains a standardised implementation of this technique. We adopt this package to build
 104 our BDT model to reject the electron contamination.

105 **3.1.1 BDT input variables**

106 Based on the difference in topology between electromagnetic and hadronic showers, we
 107 choose eight variables as inputs of the BDT model to help discriminate pion against elec-
 108 tron events. Hereafter, a description of each of these variables is given:

- 109 • **First layer of the shower (Begin):** To define the layer in which the shower starts, we
 110 look for the first layer along the incoming particle direction which contains at least
 111 4 fired pads. To eliminate fake shower starts due to accidental noise or a locally
 112 high multiplicity, the following 3 layers after the first layer are also required to have
 113 more than 4 fired pads (hits) for each of them. If no layer fulfils this, a value of -10
 114 is assigned to the variable. Since each layer of the SDHCAL represents about 1.2
 115 radiation lengths (X_0), electromagnetic showers start developing in the first layers.
 116 For pions, their interaction probability density is given by $1 - \exp(-\frac{l}{\lambda_l})$ where l
 117 is the length of the pion trajectory in the calorimeter medium before interacting.
 118 Figure 3 shows the distribution of the first layer of the shower in the SDHCAL
 119 prototype for pions and electrons as obtained from the simulation.
- 120 • **Number of track segments in the shower (nTrack):** Applying the Hough Trans-
 121 form (HT) method to single out the tracks in each event as described in Ref. [13],

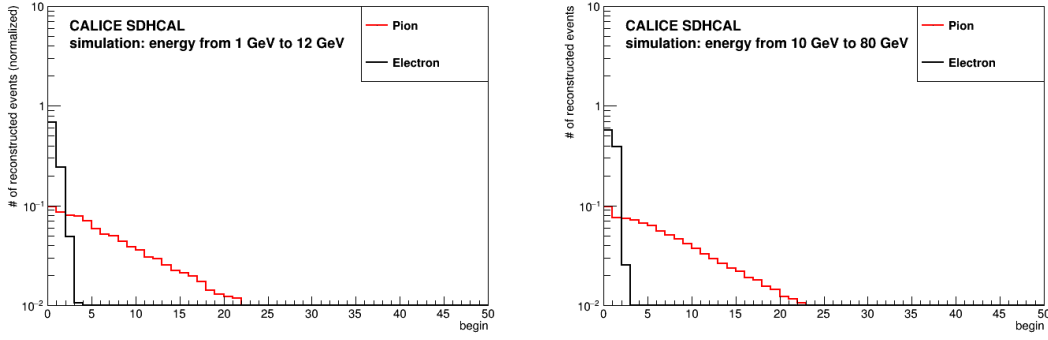


Figure 3. Distribution of the first layer number of pion and electron showers in the PS energy range of 1-12 GeV (left) and the SPS energy range of 10-80 GeV (right) of pions and electrons as given by the simulation. The red line corresponds to pions and the black one to electrons.

122 we obtain the number of track segments in the pion, electron and muon events. A
 123 HT-based segment candidate is considered as a track segment if there are more than
 124 6 aligned hits with not more than one layer separating two consecutive hits. Electron
 125 showers feature almost no track segment while most of the hadronic showers have
 at least one. The distribution of nTrack can be seen in Fig. 4

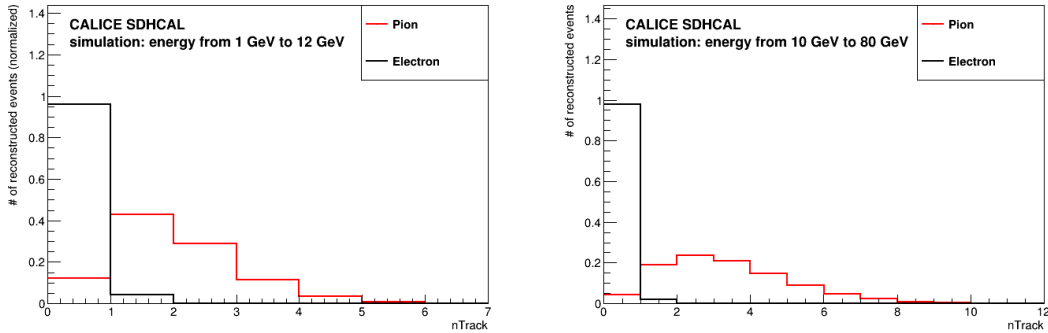


Figure 4. Distribution of the number of track segments in pion and electron showers in the PS energy range of 1-12 GeV (left) and the SPS energy of 10-80 GeV (right) as given by the simulation. The red line corresponds to pions and the black one to electrons.

126

127 • **Number of clusters of the shower (nCluster):** All hits in a given layer are clustered
 128 using a nearest-neighboring algorithm described in Ref. [1]. It consists in merging
 129 in each GRPC plate the hits sharing a common edge. This variable defines the
 130 number of clusters of the shower and its distribution is shown in Fig. 5. Indeed, the
 131 compactness of the electromagnetic shower leads to a reduced number of clusters in
 132 an electron shower with respect to that of a pion shower of the same energy.

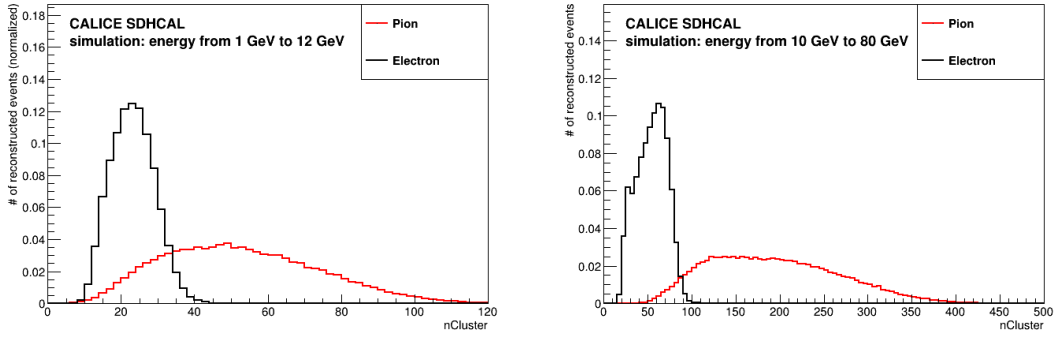


Figure 5. Distribution of the number of clusters in pion and electron showers in the PS energy range of 1-12 GeV (left) and the SPS range of 10-80 GeV (right) as given by the simulation. The red line corresponds to pions and the black one to electrons.

- 133 • **Ratio of the number of shower layers over the total number of fired layers**

134 **($n_{\text{InteractingLayers}}/n_{\text{Layers}}$):** This is the ratio between the number of the shower

135 layers defined as those in which the Root Mean Square (RMS) of the hits' position in

136 the x - y plane exceeds 5 cm in both x and y directions and the total number of layers

137 with at least one hit. This variable allows, as can be seen in Fig. 6, a good separation

138 between pions and electrons at low energy. It also allows an easy discrimination

139 of muons (including the radiative ones) against pions and electrons ones as will be

shown later.

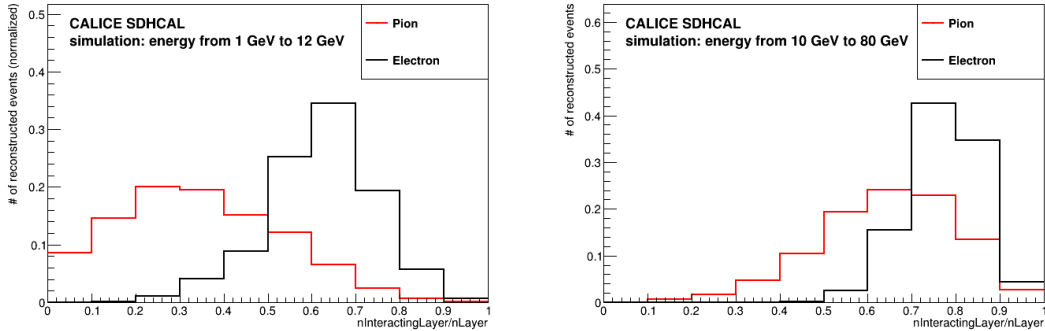


Figure 6. Distribution of the ratio of number of shower layers over the total number of fired layers in pion and electron showers in the PS energy range of 1-12 GeV (left) and the SPS energy range of 10-80 GeV (right) as given by the simulation. The red line corresponds to pions and the black one to electrons.

- 140

141 • **The average number of hits per fired layers ($n_{\text{Hit}}/n_{\text{Layer}}$):** This is the ratio

142 between the total number of fired pads over the number of layers with at least one

143 fired pad. The distribution of this variable is shown in Fig. 7.

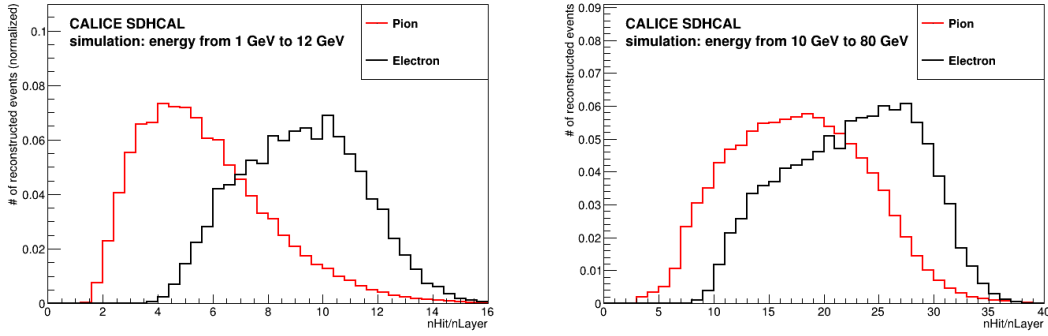


Figure 7. Distribution of the average number of hits per fired layers in pion and electron showers in the PS energy range of 1-12 GeV (left) and the SPS range of 10-80 GeV (right) as given by the simulation. The red line corresponds to pions and the black one to electrons.

- 144 • **Shower density (Density):** This is the average number of the neighbouring hits
 145 located in the 3×3 pads around one of the hits (including the hit itself) in the given
 146 event. Figure 8 shows clearly that electromagnetic showers are more compact than
 147 the hadronic ones as expected.

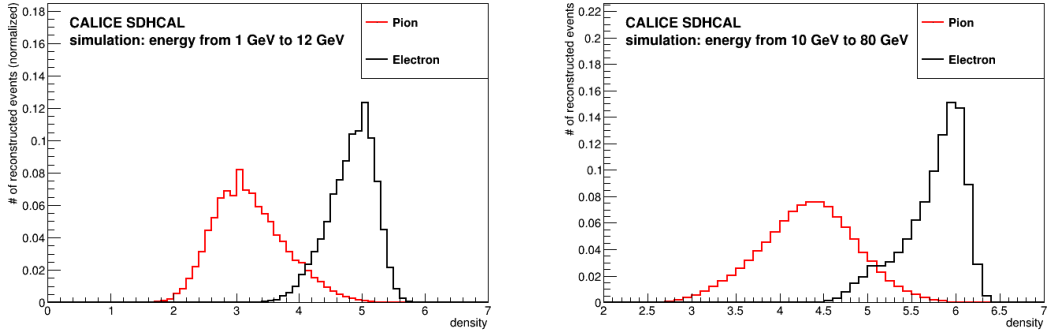


Figure 8. Distribution of the density of pion and electron showers in the PS energy range of 1-12 GeV (left) and the SPS range of 10-80 GeV (right) as given by the simulation. The red line corresponds to pions and the black one to electrons.

- 148 • **Shower radius (meanRadius):** This is the RMS of hits distance with respect to the
 149 event axis. To estimate the event axis, the average positions of the hits in each of
 150 the ten first fired layers of an event are used to fit a straight line. The straight line is
 151 then used as the event axis. The electromagnetic shower being more compact than
 152 the hadronic shower, its radius is expected to be smaller as can be seen in Fig. 9.
- 153 • **Ratio of the number of third-threshold hits over the total number of hits (nHit3/nHit):**
 154 The three thresholds indicate the amount of charge collected in each pickup pad. The

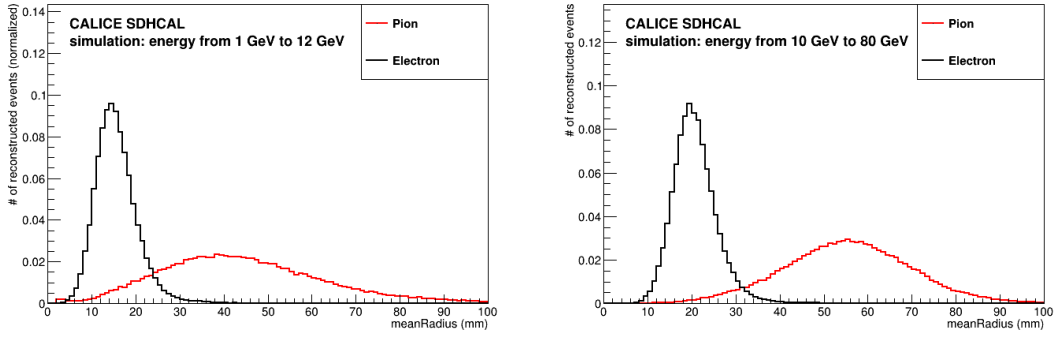


Figure 9. Distribution of the meanRadius of pion and electron showers in the PS energy range of 1-12 GeV (left) and the SPS range of 10-80 GeV (right) as given by the simulation. The red line corresponds to pions and the black one to electrons.

155 third one is set to single out the pads with high collected charge that may be induced
 156 by the passage of many particles in the cell associated to the pickup pad. The nHit3
 157 is the number of third-threshold hits in one event. The ratio of nHit3 to the total
 158 number of hits helps to distinguish electromagnetic-like events and separate them
 159 from hadronic-like ones since the relative number of hits with the third threshold is
 160 higher in the former than in the latter due to the difference of their compactness. The
 161 distribution of this ratio can be seen in Fig. 10.

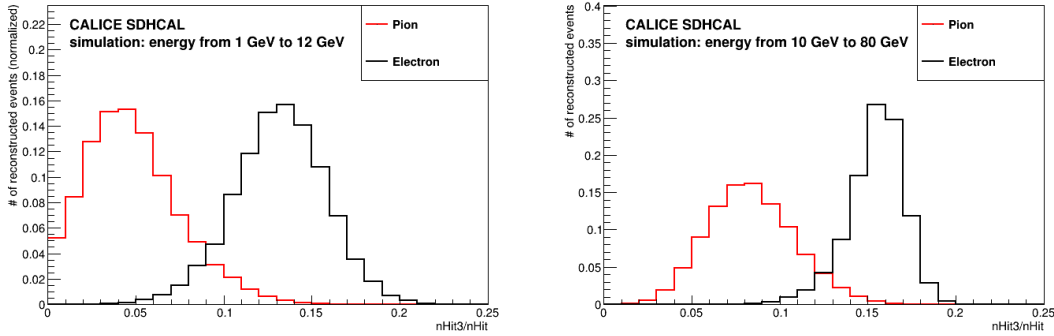


Figure 10. Distribution of the ratio of number of third threshold hits over the total number of hits in pion and electron showers in the PS energy range of 1-12 GeV (left) and the SPS range of 10-80 GeV (right) as given by the simulation. The red line corresponds to pions and the black one to electrons.

162 3.1.2 Training and testing details of the BDT

163 For the training and testing process, 200000 pion and 200000 electron simulated events
 164 are used to form a training set (66.7%) and a testing one (33.3%). Another independent

Table 1. The chosen BDT hyperparameters.

Option	Setting
Ntrees (Number of trees in the forest)	1000
nCuts (Number of steps during node cut optimisation)	20
MaxDepth (Max depth of the decision tree allowed)	4

165 400000 events including pions and electrons are used as a validation set. The events are
166 simulated evenly in the energy interval between 1 and 80 GeV. The hyperparameters re-
167 sulting from the BDT optimisation procedure such as `maxDepth`¹ are described in Table 1.
168 After feeding the eight topological variables to the BDT model using the training and test-
169 ing sets, the performance of our model is shown in Fig. 11. It clearly shows the strong
170 separation power between pions and electrons. At the same time, the BDT response of the
171 validation sets has very good agreement with training ones. This confirms that our model
172 is performing very well and is not subject to overfitting. After applying the muon rejection
173 cuts to be explained in section to our in section 3.2 to our collected data, we apply our
174 BDT models on the selected events. Figure 12 shows the BDT output of 6 GeV (left plot)
175 and 11 GeV (right plot) pion runs which are supposed to be free of electron contamination.
176 The performance of the pion event selection matches the one obtained with the simulated
177 pion events quite well as shown in this figure, thus confirming that our model is reliable.
178 Figure 13 shows the result of 3 GeV and 5 GeV pion beam runs which, in principle, may
179 contain electron contamination. From this figure, one can see that most of the events are
180 located in the region associated to pions and a good agreement is observed between the
181 data and the simulation even in the region of overlap between the pions and the electrons.
182 Therefore, the electron contamination in pion runs in the 3-5 GeV energy range is rather
183 small even if it is more important than that of the PS higher energy runs. By requiring the
184 BDT response to be larger than 0.0, we select pure pion events.

185 3.2 Muon contamination rejection

186 The main contamination in our beam data is that of muons, including beam muons and
187 cosmic ones. To eliminate these two kinds of muons, we use the information based on
188 the different behaviours of muons and pions in the SDHCAL prototype. Basically, muons
189 cross the prototype and only leave a straight track in the prototype like the one shown in
190 Fig. 14. The mean of hits distance (described by the variable `meanRadius` hereafter) of
191 muon hits with respect to the global event axis is thus very often less than 1.5 cm (≈ 1.5
192 pads) as shown in Fig. 15.

193 To eliminate most of the muon contamination, we require that the `meanRadius` is
194 greater than 2 cm. To further reduce the muon contamination, including the so-called
195 radiative muons that produce a few hit clusters around the muon track, we require the ratio

¹It controls the maximum depth of the tree that will be created. It can also be described as the length of the longest path from the tree root to a leaf. The root node is considered to have a depth of 0.

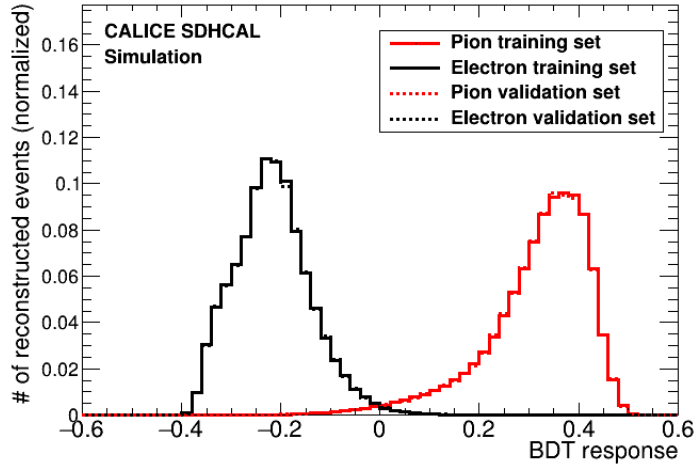


Figure 11. Distribution of the BDT output of training and validation set using the simulated electron (black) and pion (red) events from 1 GeV to 80 GeV. The solid line is from training set while the dashed one is from validation set.

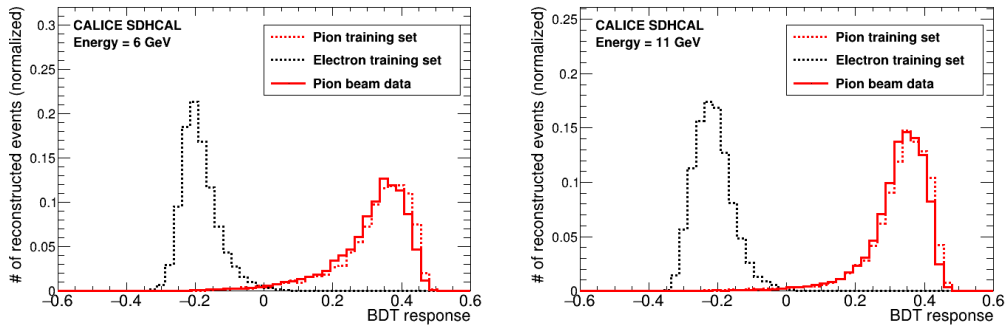


Figure 12. The BDT output of 6 GeV (left) and 11 GeV (right) beam runs after muon rejection. The solid line is from pion beams and dashed one is from training set.

196 of the number of shower layers to the total number of layers with at least one hit to be
 197 more than half.

198 To check the rejection power of the muon cuts, we apply it to dedicated muon runs.
 199 Figure 16 shows the distribution of the number of hits before and after muon rejection for
 200 120 GeV muon runs. It clearly shows the rejection power of this selection which is higher
 201 than 99.0%.

202 The result of the selection including the muon rejection and electron cut (BDT re-
 203 sponse > 0.0) is shown in Fig. 17 and Fig. 18 for PS and SPS beam data runs respectively.

204

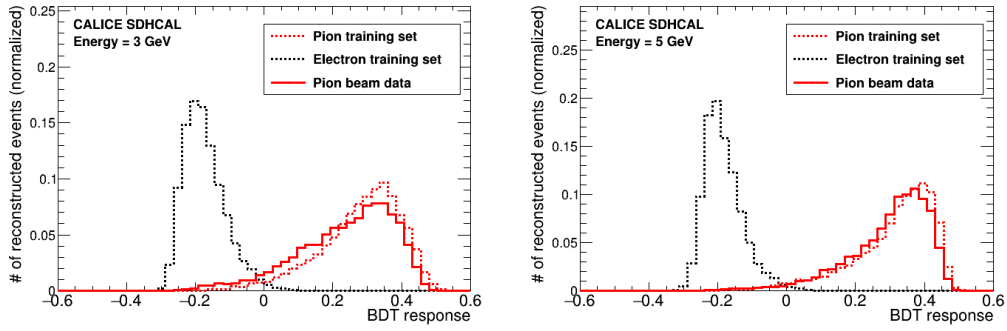


Figure 13. The BDT output of 3 GeV (left) and 5 GeV (right) beam runs after muon rejection. The solid line is from pion beams and dashed one is from training set.

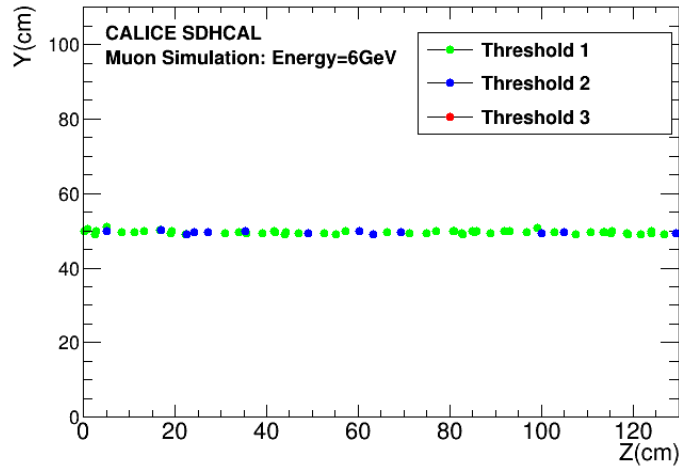


Figure 14. Event display of one 6 GeV simulated muon with the green, blue and red colour indicating the first, second and third threshold hits respectively. The third threshold is often absent in muon tracks because of the small amount of charge produced by muons in the RPC.

205 4. Energy reconstruction

206 The rejection of electrons present in the pion data sample using the BDT but also that of
 207 the muons allows us to have pure pion sample as explained in the previous section. The
 208 selected pion events of the PS beam energy from 3 GeV to 11 GeV and those in the range
 209 of 10-80 GeV of the SPS, can then be used to reconstruct energy.

210 Based on the information of the number of hits belonging to first threshold ($nHit1$),
 211 second threshold ($nHit2$) and third threshold ($nHit3$), the hadronic shower energy can be
 212 reconstructed as described in Ref. [6] using the following formula:

$$E_{reco} = \alpha \times nHit1 + \beta \times nHit2 + \gamma \times nHit3 \quad (4.1)$$

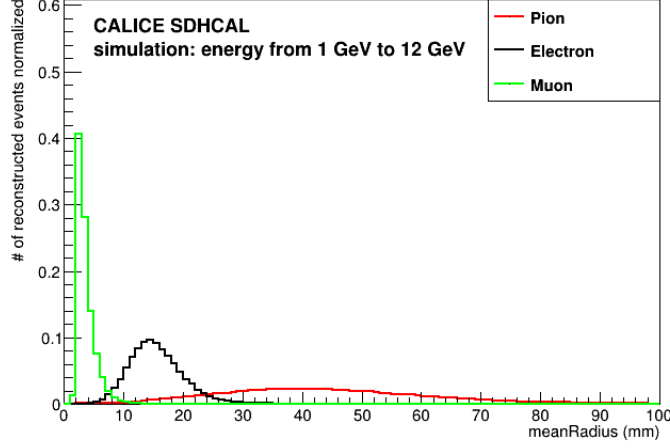


Figure 15. Distribution of the meanRadius of shower by 1 GeV to 12 GeV muons as given by the simulation (green). Electrons(black) and pions(red) meanRadius distributions are also shown.

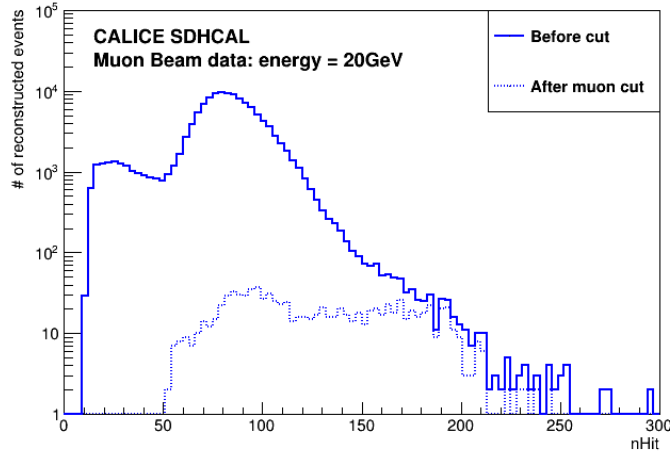


Figure 16. Distribution of the number of hits for 20 GeV muon run before (solid line) and after (dashed line) muon cut.

213 where α , β and γ are weight factors which are parametrised as second order polynomials
 214 of the total number of hits $nHit = nHit1 + nHit2 + nHit3$:

$$\begin{aligned}
 \alpha &= \alpha_1 + \alpha_2 \times nHit + \alpha_3 \times nHit^2 \\
 \beta &= \beta_1 + \beta_2 \times nHit + \beta_3 \times nHit^2 \\
 \gamma &= \gamma_1 + \gamma_2 \times nHit + \gamma_3 \times nHit^2
 \end{aligned}
 \tag{4.2}$$

215 The nine parameters $\alpha_{i=1,2,3}$, $\beta_{j=1,2,3}$ and $\gamma_{k=1,2,3}$ are obtained, as described in Ref. [6],
 216 from a part of the data samples of a few energy points by minimising the following χ^2

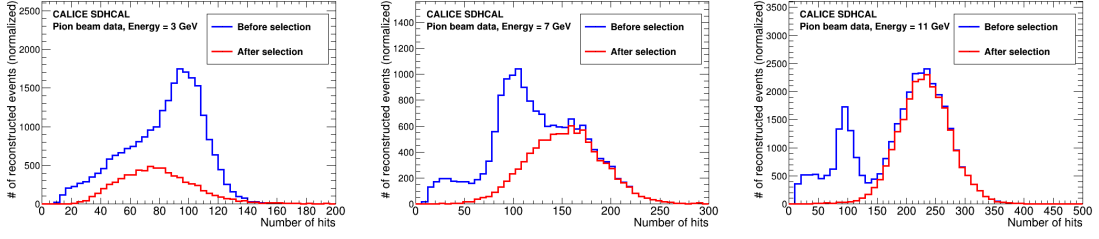


Figure 17. The number of hits for 3, 7 and 11 GeV pion beam runs before (blue) and after (red) muon selection.

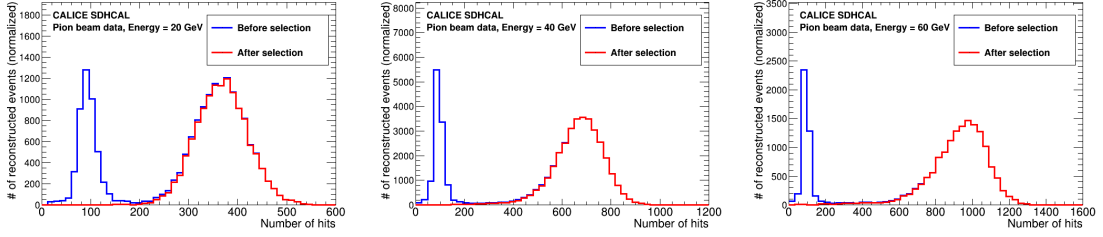


Figure 18. The number of hits for 20, 40 and 60 GeV pion beam runs before (blue) and after (red) muon selection.

217 expression:

$$\chi^2 = \sum_{i=1}^N \frac{(E_{beam}^i - E_{reco}^i)^2}{\sigma_i^2} \quad (4.3)$$

218 where the E_{beam}^i denotes the beam energy and the E_{reco}^i is the reconstructed energy. N is the
 219 number of total events and $\sigma_i = \sqrt{E_{beam}^i}$ where the choice of $\sigma = \sqrt{E_{beam}^i}$ is motivated by
 220 the fact that the expected energy resolution is approximately given by the stochastic term:

$$221 \frac{\sigma}{E_{beam}} = \frac{\alpha}{\sqrt{E_{beam}}}.$$

222 Since the PS raw 10 GeV sample is almost free of electron contamination, it is there-
 223 fore expected to be less impacted by the BDT-based selection. On the contrary, the SPS
 224 raw 10 GeV sample electron contamination is relatively higher and could thus be impacted
 225 by the BDT-based selection. To check however that this selection only eliminates the elec-
 226 trons without changing the pion sample characteristics, the reconstructed energy of the PS
 227 10 GeV sample without BDT selection is compared to that of the SPS one after applying
 228 the BDT selection. Fig. 19 shows the normalised reconstructed energy distribution of these
 229 two samples. The good agreement between the two distributions confirms the absence of
 230 bias of the BDT selection and its efficiency in rejecting the electron contamination

231 4.1 Energy resolution and linearity

232 The two purified samples; the one of 3-11 GeV and the one of 10-80 GeV collected at the
 233 PS and the SPS beamline respectively, are then used to reconstruct the pion energy in the

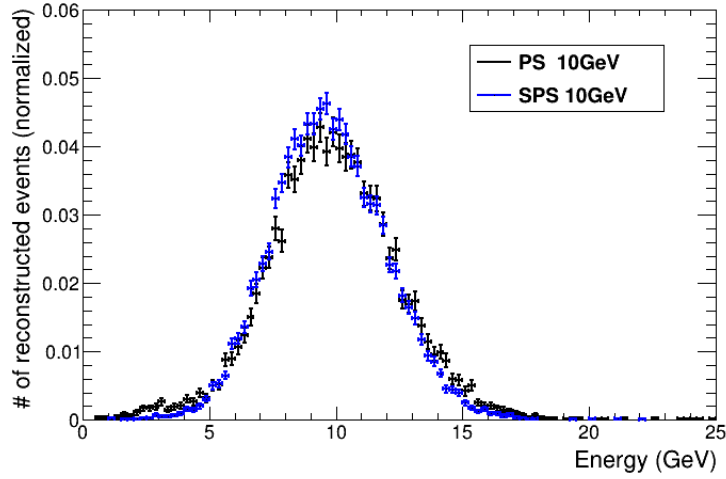


Figure 19. Reconstructed energy of the the PS 10 GeV pion sample and that of the SPS 10 GeV sample after applying the BDT selection on the latter.

234 SDHCAL following the method described in Ref. [6].

235 The reconstructed energy distributions of 3, 7 and 11 GeV pion data samples collected
 236 at PS are shown in Fig. 20 .

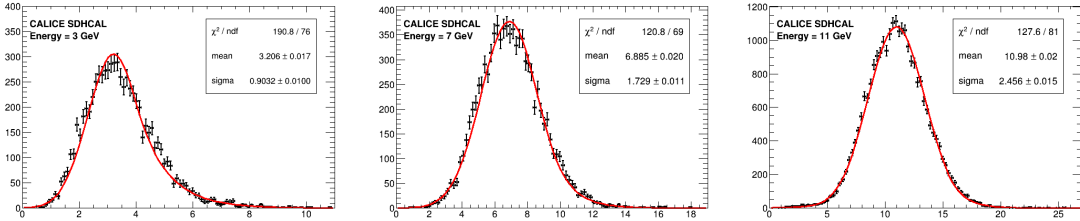


Figure 20. Reconstructed energy distributions for 3 (left), 7 (middle) and 11 GeV (right) pion data samples collected at the PS. The distributions are fitted with a double sided Crystal Ball function. The variance of the Gaussian part of the Crystal Ball function is used to estimate the resolution of the reconstructed energy.

237 The reconstructed energy distributions of 20, 40 and 60 GeV pion data samples col-
 238 lected at SPS are shown in Fig. 21 .

239 After fitting the reconstructed energy distribution from 3 to 80 GeV, the mean value
 240 and standard deviation of the Gaussian function are taken as the reconstructed energy and
 241 its resolution respectively. In Fig. 22, the energy linearity (left) and resolution results
 242 (right) are shown using both PS and SPS data.

243 The same procedure is applied to the SPS sample only. Similar results as the one
 244 obtained with both PS and SPS beamlines are obtained as can be shown in Fig. 23. More

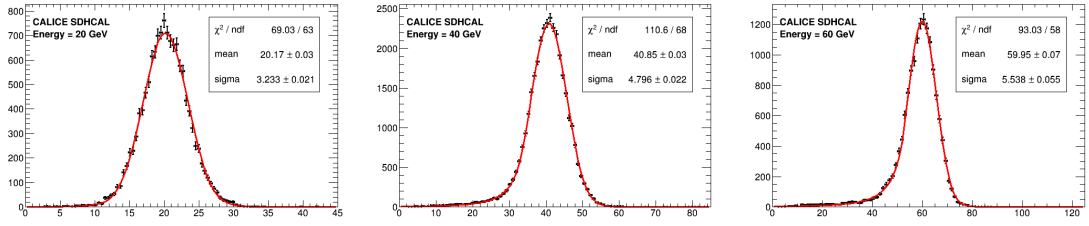


Figure 21. Reconstructed energy distributions for 20 (left), 40 (middle) and 60 GeV (right) pion data samples collected at SPS. The distributions are fitted with a double-sided Crystal Ball function. The variance of the Gaussian part of the Crystal Ball function is used to estimate the resolution of the reconstructed energy.

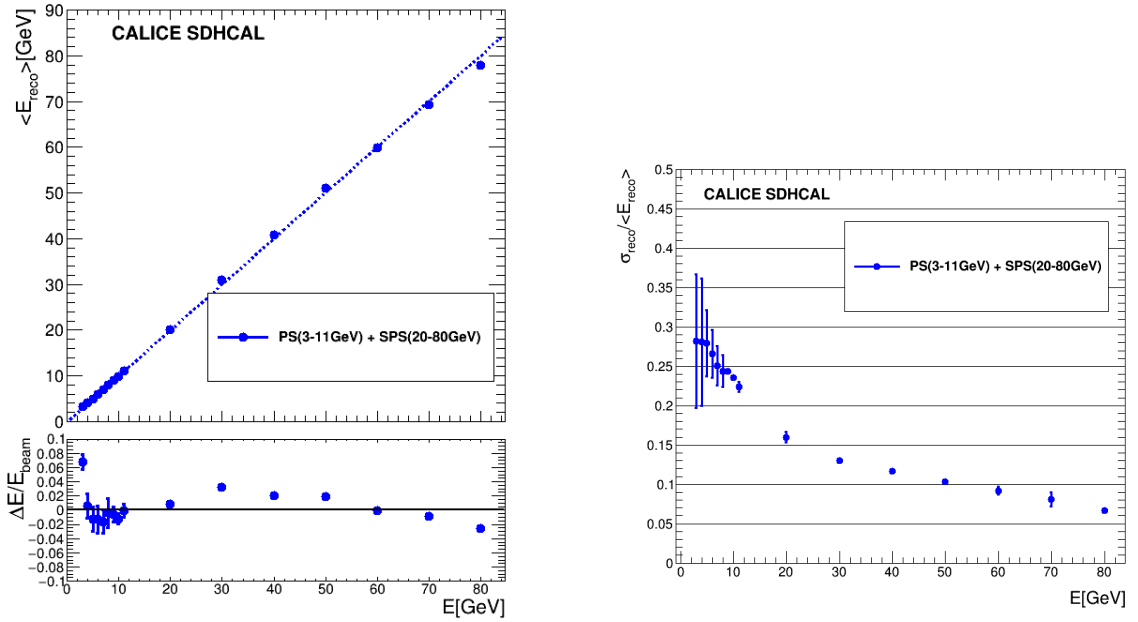


Figure 22. Mean reconstructed energy of pion showers as a function of the beam energy as well as relative deviation of the pion mean reconstructed energy with respect to the beam energy (left) and resolution of the reconstructed hadron energy as a function of the beam energy (right). Both statistical and systematic uncertainties are included in the error bars. Dashed line on the left plot indicates the ideal linearity response of the calorimeter.

245 importantly, these SPS results are similar to those obtained in 2012 [6]. This confirms the
 246 robustness of the SDHCAL prototype over time.

247 5. Uncertainties estimation

248 The linearity and energy resolution results presented in section. 4.1 include statistical and
 249 systematic uncertainties. We present here after the main contributions to the systematic

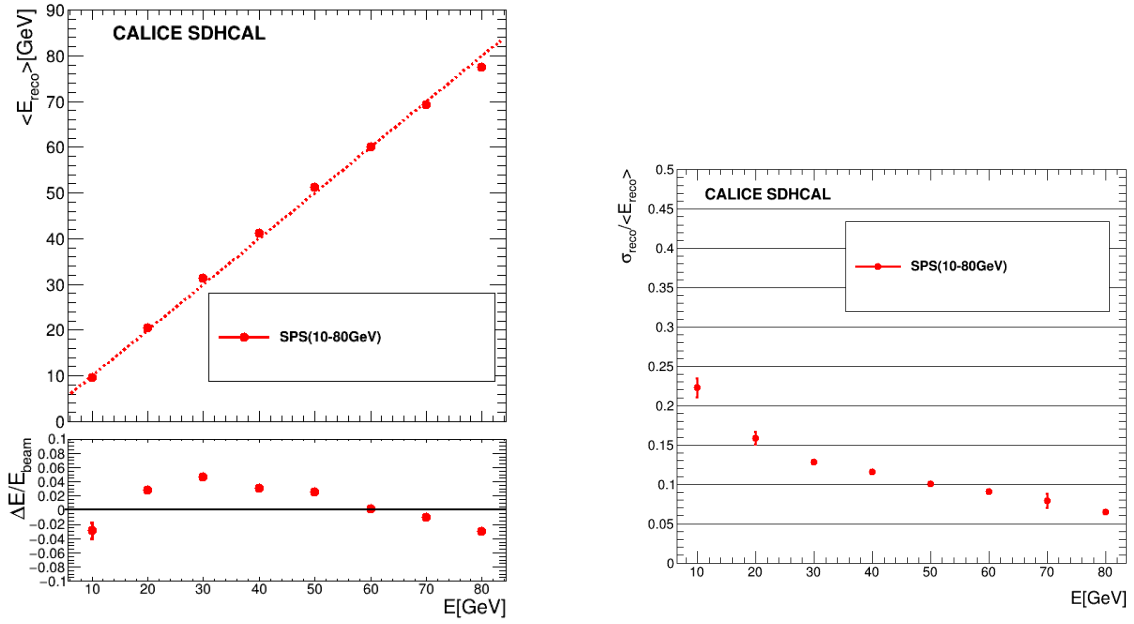


Figure 23. Mean reconstructed energy for pion showers as a function of the beam energy as well as relative deviation of the pion mean reconstructed energy with respect to the beam energy (left) and resolution of the reconstructed hadron energy as a function of the beam energy (right). Both statistical and systematic uncertainties are included in the error bars. Dashed line on the left plot indicates the ideal linearity response of the calorimeter.

250 uncertainties:

- 251 • For the reconstructed energy of all energy points, a double sided Crystal Ball fit func-
252 tion and a Gaussian fit function are used. The difference of fitting results obtained
253 from these two fit functions are considered as the value of systematic uncertainties
254 associated to the fit of the reconstructed energy.
- 255 • For the muon rejection, using all energy points data samples of PS, the meanRadius
256 varied by an arbitrary 5% in both directions with respect to the nominal values. The
257 maximum deviation with respect to the nominal value is used as an estimate of the
258 systematic uncertainties due to a residual muon contamination.
- 259 • For the electron rejection using the BDT method, the BDT cut value is changed
260 from -0.05 to 0.05 with respect to the nominal values 0.0. The maximum deviations
261 are taken and added to the systematic uncertainties as an estimate of the impact of
262 residual electron contamination.

263 Although the statistical uncertainties are found to be negligible for almost all the runs
264 with respect to systematic uncertainties, their contributions as well as the systematic un-
265 certainties previously discussed are added quadratically to obtain the final uncertainties.

266 The results are summarised in Tables 2 and 3. The uncertainty coming from the different
 267 fit functions is found to be the main component of total systematic uncertainties.

Energy(GeV)	Beam data of PS and SPS
3	0.068 ± 0.011
4	0.006 ± 0.017
5	-0.013 ± 0.017
6	-0.013 ± 0.019
7	-0.016 ± 0.016
8	-0.004 ± 0.021
9	-0.006 ± 0.010
10	-0.012 ± 0.007
11	-0.001 ± 0.009
20	0.009 ± 0.001
30	0.032 ± 0.001
40	0.021 ± 0.001
50	0.019 ± 0.001
60	-0.001 ± 0.001
70	-0.010 ± 0.001
80	-0.027 ± 0.001

Table 2. List of $\frac{\Delta E}{E}$ observed and associated uncertainties for beam data in the energy range from 3 to 80 GeV.

268 6. Conclusion

269 The data collected from the exposure of the SDHCAL prototype to pion beams in both PS
 270 and SPS covering a large range of energy (3-80 GeV) are analyzed. Rejection of muon
 271 and electron contamination is performed. For the latter a BDT-based technique is applied.
 272 This technique allows the rejection of the electron contamination without reducing the
 273 pion sample compared to the analysis used in Ref. [6] where the electron contamination
 274 was reduced by requiring the interaction to start showering after ten radiation lengths (X_0)
 275 leading to a loss of about half of the pion events. Energy of the pions collected in both
 276 PS and SPS is then reconstructed following the techniques developed in Ref. [6] and com-
 277 pared with those obtained with the SPS data only and with those obtained with those of
 278 2012 following a standard selection analysis. The results show that good performances in-
 279 cluding excellent linearity and energy resolution, are obtained over a large dynamic range
 280 from 3 to 80 GeV.

Energy(GeV)	Beam data of PS and SPS
3	0.282 ± 0.085
4	0.281 ± 0.081
5	0.279 ± 0.042
6	0.266 ± 0.030
7	0.251 ± 0.025
8	0.244 ± 0.020
9	0.244 ± 0.001
10	0.236 ± 0.001
11	0.224 ± 0.006
20	0.160 ± 0.007
30	0.130 ± 0.001
40	0.117 ± 0.001
50	0.103 ± 0.002
60	0.092 ± 0.005
70	0.081 ± 0.009
80	0.067 ± 0.001

Table 3. List of energy resolution observed and associated uncertainties for beam data in the energy range from 3 to 80 GeV.

281 7. Acknowledgements

282 This study was supported by the French ANR agency (DHCAL Grant) and the CNRS-
283 IN2P3; by the MCIN/AEI and the Programa Estatal de Fomento de la Investigación Ci-
284 entífica y Técnica de Excelencia María de Maeztu, grant MMDM-2015-0509; by the Na-
285 tional Natural Science Foundation of China (Grant No. 11961141006) and the National
286 Key Programmes for S&T Research and Development (Grant No. 2016YFA0400404); by
287 the National Research Foundation of Korea, Grant Agreement 2019R111A3A01056616.
288 The authors would also like to thank the CERN accelerator staff for their precious help in
289 preparing both the PS and the SPS beams.

290 References

- 291 [1] G. Baulieu et al., Construction and commissioning of a technological prototype of a
292 high-granularity semi-digital hadronic calorimeter, *JINST* **10** (2015) P10039.
- 293 [2] M. A. Thomson, Particle Flow Calorimetry and the PandoraPFA Algorithm, *NIMA* **611 25**
294 (2009), arXiv:0907.3577
- 295 [3] V. L. Morgunov, Calorimetry design with energy-flow concept (imaging detector for
296 high-energy physics), in Proc of Int. Conf. on Calorimetry (Calor02), (2002) Pasadena, 70.

- 297 [4] J. C. Brient and H. Videau, The calorimetry at the future e+e- linear collider, in Proc. of
298 APS/DPP/DBP summer study on the future of particle physics, (2002) Snowmass, Colorado
299 [hep-ex/0202004].
- 300 [5] F. Dulucp, C. de La Taille, G. Martin-Chassard, N. Seguin-Moreau, HARDROC: Readout
301 chip for CALICE/EUDET Digital Hadronic Calorimeter, IEEE Nuclear Science Symposium
302 & Medical Imaging Conference, IEEE, 2010.
- 303 [6] CALICE collaboration, First results of the CALICE SDHCAL technological prototype,
304 JINST **11** (2016) P04001.
- 305 [7] S. Agostinelli et al. GEANT4 - a simulation toolkit, NIMA **506** (2003) 250-303.
- 306 [8] CALICE collaboration, Resistive Plate Chamber Digitization in a Hadronic Shower
307 Environment, JINST **11** (2016) P06014, arXiv:1604.04550.
- 308 [9] B. P. Roe, H. J. Yang, J. Zhu et al., Boosted decision trees as an alternative to artificial neural
309 networks for particle identification, NIMA **543** (2004) 577-584.
- 310 [10] H. J. Yang, B. P. Roe, J. Zhu et al., Studies of boosted decision trees for MiniBooNE particle
311 identification, NIMA **555** (2005) 370-385.
- 312 [11] CALICE Collaboration, Hadron selection using Boosted Decision Trees in the semi-digital
313 hadronic calorimeter , <https://inspirehep.net/record/1718039>.
- 314 [12] A. Hoecker, P. Speckmayer, J. Stelzer, J. Therhaag, E. von Toerne and H. Voss,
315 TMVA-Toolkit for multi data analysis, arXiv:physics/0703039.
- 316 [13] CALICE collaboration. "Tracking within Hadronic Showers in the CALICE SDHCAL
317 prototype using a Hough Transform Technique." arXiv preprint arXiv:1702.08082 (2017).